

RESEARCH ARTICLE | MAY 22 2025

Annealing effects on crystalline quality and device performance of ultrawide bandgap h-BN quasi-bulk crystals



N. K. Hossain ; G. Somasundaram ; Z. Alemoush ; J. Li ; J. Y. Lin ; H. X. Jiang

Check for updates

Appl. Phys. Lett. 126, 202107 (2025)

<https://doi.org/10.1063/5.0260647>



Articles You May Be Interested In

Status of h-BN quasi-bulk crystals and high efficiency neutron detectors

J. Appl. Phys. (May 2024)

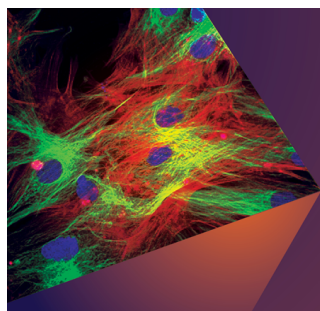
Transport properties of h-BN lateral devices

Appl. Phys. Lett. (January 2025)

Properties of photocurrent and metal contacts of highly resistive ultrawide bandgap semiconductors

Appl. Phys. Lett. (April 2024)

28 May 2025 16:43:01



Applied Physics Letters
**Special Topics Open
 for Submissions**
[Learn More](#)



Annealing effects on crystalline quality and device performance of ultrawide bandgap h-BN quasi-bulk crystals

Cite as: Appl. Phys. Lett. **126**, 202107 (2025); doi: [10.1063/5.0260647](https://doi.org/10.1063/5.0260647)

Submitted: 17 February 2025 · Accepted: 8 May 2025 ·

Published Online: 22 May 2025



View Online



Export Citation



CrossMark

N. K. Hossain,^{a)}  G. Somasundaram,  Z. Alemoush,  J. Li,  J. Y. Lin,  and H. X. Jiang 

AFFILIATIONS

Department of Electrical and Computer Engineering, Texas Tech University, Lubbock, Texas 79409, USA

^{a)} Author to whom correspondence should be addressed: khossain@ttu.edu

ABSTRACT

Hexagonal boron nitride (h-BN) is a notable member of ultrawide bandgap semiconductors, distinguished by its unique layered crystalline structure and exceptional electrical and optical properties. One of the established and important device applications of h-BN lies in solid-state neutron detectors. Achieving high detection efficiency requires thick, high-quality crystals to maximize neutron interactions and charge carrier collection. While hydride vapor phase epitaxy (HVPE) excels at growing thick, uniform h-BN films (quasi-bulk wafers), its high growth rate can compromise crystallinity by introducing structural defects. This study investigates the impact of post-growth high-temperature annealing (up to 1900 °C) on 1 mm thick HVPE-grown h-BN. X-ray diffraction confirmed significant improvements in crystallinity with higher annealing temperatures, leading to increased resistivity and an enhanced charge carrier mobility-lifetime product. A detector fabricated from h-BN annealed at 1900 °C demonstrated a 0.7% overall detection efficiency and 37% charge collection efficiency for fast neutrons from an AmBe source. These findings highlight post-growth annealing as a simple yet highly effective method to improve h-BN quality for a wide range of applications, including direct conversion solid-state neutron detectors, which are becoming increasingly vital in various nuclear diagnostic instruments.

Published under an exclusive license by AIP Publishing. <https://doi.org/10.1063/5.0260647>

The development of III-nitride wide bandgap (WBG) semiconductor technology has revolutionized applications ranging from lighting and consumer electronics to power electronics.^{1–4} Within the nitride family, hexagonal boron nitride (h-BN) is known for its ultrawide bandgap (UWBG) of approximately ~6.1 eV (Refs. 5 and 6) and high breakdown field of ~12 MV cm⁻¹.⁷ Despite its exceptional properties, h-BN is relatively less explored compared to other materials in the nitride family. While few-layer h-BN has gained traction as a dielectric substrate and gate material in two-dimensional electronics^{8–10} and as a host for single photon emitters,¹¹ the development of large-diameter bulk h-BN remains underexplored but is necessary for technologically significant device applications. Previously, high pressure high temperature (HPHT)^{6,12–15} and catalytic metal flux solution methods^{16–18} have been successful in producing high-quality millimeter-sized single crystal bulk h-BN, the long growth hours translate to high costs and their limitation for fabricating millimeter-sized structures restricts their practical application in devices based on bulk h-BN crystals.

One distinctive feature of h-BN among nitride semiconductors is the significant nuclear interaction cross section of approximately 3480

barns between thermal neutrons and its Boron-10 (¹⁰B) isotope constituent.¹⁹ This corresponds to a mean free path of 47.3 and 237 μm for thermal neutrons in B-10 enriched (h-¹⁰BN) and natural h-BN, respectively,^{20–25} which means that the development of h-¹⁰BN and h-BN crystals with a thickness greater than 47.3 and 237 μm, respectively, can provide high detection efficiencies for thermal neutrons. A record high thermal neutron detection efficiency of 60% has been attained recently by our group by developing 100 μm thick h-¹⁰BN wafers.^{23,24} In contrast, the direct detection of fast neutrons with energies above 1 MeV occurs through charge carrier generation by the elastic scattering of fast neutrons with B and N atoms, which have an interaction cross section of only about 1 barn, corresponding to a mean free path in h-BN of 7.6 cm (5.2 cm) for fast neutrons from Californium-252 (²⁵²Cf) (AmBe) neutron source.^{25,26} So, the detector thickness requirement for direct detection of fast neutrons is significantly larger than for thermal neutrons. Neutron detectors fabricated from h-BN have the potential to achieve 100% efficiency if the detector's thickness is sufficiently large and the material quality is high. The utilization of h-BN in fast neutron detectors could be groundbreaking,

as there is currently no technology available on the market for direct detection of fast neutrons with practical efficiency using semiconductors. Moreover, the development of a single h-BN material that is sensitive to both thermal and fast neutrons is anticipated to lead to the creation of innovative neutron detection technologies, offering a promising avenue for advancing neutron detection capabilities.

While the metal-organic chemical vapor deposition (MOCVD) method has been utilized for growing h-BN for thermal neutron detectors,^{20–23} its low growth rate, typically limited to below 5 $\mu\text{m}/\text{h}$, poses significant challenges in producing the required thickness for the direct detection of fast neutrons. To address these challenges, the hydride vapor phase epitaxy (HVPE) method appears to be a more viable option, as the technique has been employed to produce high-quality AlN quasi-bulk crystals at a growth rate exceeding 100 $\mu\text{m}/\text{h}$.^{27,28} Our group has previously produced 100–500 μm thick h-BN wafers using HVPE at a high growth rate of 15 $\mu\text{m}/\text{h}$.^{24–26} It was observed that the high growth rate of HVPE induces stacking disorders in thick h-BN due to its layered crystalline structure, leading to a deterioration in crystalline quality.²⁶ It is crucial to explore post-growth processes, such as annealing at high temperatures, to enhance material quality and device performance. Post-growth annealing has been proven to be an effective technique for further improving the crystalline quality of h-BN and has been employed to further improve crystalline quality of MOCVD²⁹ and molecular beam epitaxy (MBE) grown³⁰ h-BN thin epilayers. In this work, we carried out studies of the effects of high-temperature thermal annealing on the crystalline quality and electronic transport properties of 1 mm thick h-BN quasi-bulk wafers produced by the HVPE method. As-grown and annealed h-BN wafers are characterized by x-ray diffraction (XRD), I-V characteristics, and carrier mobility and lifetime. The performance of fast neutron detectors fabricated from the annealed h-BN wafers is also presented.

h-BN wafers were grown on 4-in.-diameter c-plane sapphires of by HVPE at a growth temperature of 1550 $^{\circ}\text{C}$ using boron trichloride (BCl_3) and ammonia (NH_3) as precursors for B and N, respectively, and hydrogen (H_2) as carrier gas. To grow the 1 mm thick wafer used in the present study, a growth rate of $\sim 30 \mu\text{m}/\text{h}$ was employed. After growth, the h-BN wafer self-separates from the substrate and becomes freestanding wafer due to its negative thermal expansion coefficient (TEC) and layered crystalline structure.³¹ The samples were then annealed under N_2 gas at temperatures up to 1900 $^{\circ}\text{C}$ for 60 min. An LF 20–2200 furnace with a refractory metal hot zone (Centorr Vacuum Industries) was employed to reach this temperature. The furnace consists of a tungsten mesh inductive heating element and a molybdenum (Mo) stage. The sample was placed in between two pyrolytic boron nitride (p-BN) pieces to avoid unintentional doping during annealing. N_2 gas was used to prevent decomposition at high temperatures and to minimize the out-diffusion of N atoms from h-BN wafers during the annealing process. An optical image of a freestanding 1 mm thick h-BN sample annealed at 1900 $^{\circ}\text{C}$ is shown in the inset of Fig. 1, and no change in appearance was noticed after thermal annealing. Figure 1 shows a comparison of XRD θ -2 θ scans of as-grown and annealed h-BN wafers using two different annealing temperatures (1850 and 1900 $^{\circ}\text{C}$). Previous studies have suggested that a growth temperature above 1500 $^{\circ}\text{C}$ is needed to obtain h-BN films with proper h-phase stacking, c-lattice constant, and optical properties.^{32–34}

As observed in Fig. 1, the (002) peak of both the as-grown and high-temperature thermally annealed h-BN samples is consistently

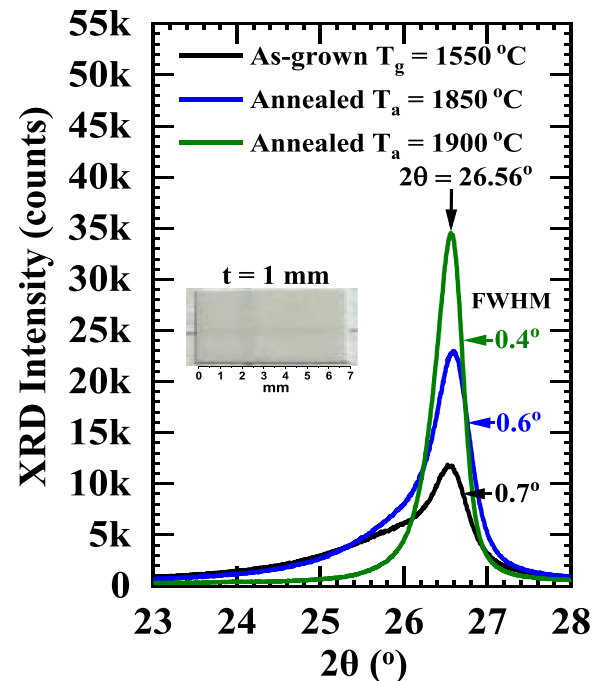


FIG. 1. Comparison of XRD patterns in 0 - 2θ scans among as-grown and annealed h-BN: As-grown $T_g = 1550 \text{ }^{\circ}\text{C}$ (black line), annealed at $1850 \text{ }^{\circ}\text{C}$ (blue line) and annealed at $1900 \text{ }^{\circ}\text{C}$ (green line), for 60 min in N_2 gas. The inset is an image of a 1 mm thick h-BN wafer annealed at $1900 \text{ }^{\circ}\text{C}$.

located at 26.56° , corresponding to a c-lattice constant of 6.7 \AA . Compared to the $100 \mu\text{m}$ thick h-BN wafers produced by HVPE by our group, this value deviates slightly more from the ideal c-lattice constant of h-BN, which is 6.66 \AA .^{24,35} The results clearly indicate that structural disorders, such as the incorporation of turbostratic-phase (t-phase) domains within h-BN, become more prevalent as the layer thickness increases during h-BN growth. Consequently, this leads to a shift in the XRD (002) peak toward lower angles from the ideal position of 26.74° . However, the XRD spectra of annealed samples clearly exhibit an enhancement in the (002) peak intensity with increasing annealing temperature. Since the (002) peak intensity is directly linked to the crystalline quality, it can be inferred that there is a proportional improvement in the crystallinity of h-BN with higher annealing temperatures.

Previous studies on h-BN have indicated the presence of domains with t-phase or (t-BN) in thick h-BN samples.^{36,37} The t-phase is characterized by random stacking or rotation of individual layers due to suboptimal growth conditions. In the XRD spectra presented in Fig. 1, the as-grown sample displays a tail on the lower angle side of the dominant (002) peak, showing the presence of an additional peak at approximately 26° due to the inclusion of t-phase domains in the sample.^{36–38} The intensity of the t-phase tail diminishes in the sample annealed at $1900 \text{ }^{\circ}\text{C}$, indicating that annealing at high temperatures promotes structural rearrangement of BN layers from t-phase to h-phase. The full-width at half maximum (FWHM) of the (002) peak also decreased from 0.7° for the as-grown sample to 0.6° and 0.4° for the sample annealed at 1850 and $1900 \text{ }^{\circ}\text{C}$, respectively. Lower FWHM means increased h-phase domain size for samples annealed at higher

temperatures. It is worth pointing out that the FWHM of the (002) peak of 100 μm thick h-BN is 0.29°.²⁴ Altogether, the results clearly demonstrate that the crystalline quality of h-BN improves significantly after the post-growth annealing process at 1900 °C. However, the (100) and (101) peaks related to the in-plane crystal structure were not observable in the XRD patterns. We believe that detecting these peaks, which are necessary for estimating the in-plane lattice constant via XRD, would require further enhancement of the long-range structural order in the c-plane.

Devices were fabricated using the as-grown and annealed h-BN samples to investigate the impact of post-growth annealing on their electrical transport properties. The samples were cut into a dimension of length $L = 5 \text{ mm}$ and width $W = 1.3 \text{ mm}$ using laser dicing and then put onto a sapphire using insulating polyimide tape. Metal contacts consisting of a bi-layer of Ni (100 nm)/Au (40 nm) were deposited on the two long edges of the diced samples using e-beam evaporation to form lateral detectors. It is important to note that the lateral device configuration was chosen to leverage the superior in-plane transport properties of h-BN over its vertical transport properties.^{20–24} The electrical characteristics were evaluated by measuring the I–V curves in both dark conditions and under photoexcitation for the as-grown and annealed samples. Dark currents, which are indicative of dark resistivity, are primarily influenced by the background carrier concentrations in the materials. In applications such as detectors, a lower dark current or higher electrical resistivity leads to an enhanced signal-to-noise ratio. The I–V curve depicted in Fig. 2 was used to calculate dark resistivity, revealing a value of $3.9 \times 10^{13} \Omega\text{cm}$ for the as-grown sample (black squares), consistent with previously reported

resistivity values for HVPE-grown h-BN wafer of 100 μm in thickness.³⁵ However, Fig. 2 shows that resistivity increases with increasing annealing temperature. Specifically, the resistivity of the material increases by nearly an order of magnitude to $2.4 \times 10^{14} \Omega\text{cm}$ for the sample annealed at 1900 °C, as shown in the dark I–V curve in Fig. 2 (green squares). In a previous study, we presented evidence that the dark resistivity of h-BN produced by HVPE at a growth rate around 15 $\mu\text{m}/\text{h}$ is controlled by the presence of boron vacancy and hydrogen complex ($V_{\text{B}}\text{--H}$) defects.³⁹ A possible scenario is that annealing drives the hydrogen out of the material, leading to a reduction in ($V_{\text{B}}\text{--H}$) complexes and an increase in the electrical resistivity. In the present study, nitrogen vacancies (V_{N}) are equally likely to be incorporated due to the use of an even higher growth rate of $\sim 30 \mu\text{m}/\text{h}$. During high-temperature annealing under N_2 , it is also possible that N_2 gas supplies N atoms slightly to fill up a fraction of V_{N} inside h-BN. Overall, the results appear to suggest that high-temperature annealing under N_2 reduces the concentrations of native defects, improves the crystalline quality of the material, and increases the resistivity of h-BN.

The mobility-lifetime ($\mu\tau$) product is a crucial carrier transport property that plays a significant role in determining the charge collection efficiency in radiation detectors. In neutron detectors, effective collection of neutron-generated charge carriers occurs when the carrier recombination time (τ) exceeds the carrier transit time (τ_t) or when the drift length of the charge carriers ($\mu\tau E$) is greater than the transit distance between the electrodes (W), expressed as $\mu\tau E \gg W$, where E represents the applied electric field. The value of the $\mu\tau$ product is highly dependent on the material's quality and purity and has a direct impact on the detector's performance. To assess the $\mu\tau$ product, measurements were conducted on both the as-grown and annealed h-BN samples by studying the bias voltage dependence of the photocurrent ranging from 0 to 500 V. A broad UV light source (180–400 nm) was employed for photoexcitation of charge carriers. Figure 3 plots the bias voltage dependence of the photocurrent for the detector fabricated from the as-grown sample (black squares), the sample thermally annealed at 1850 °C (blue squares), and the sample thermally annealed at 1900 °C (green squares).

The measured photocurrent characteristics were analyzed using a modified classical Many's equation for partial blocking metal contacts,

$$I(V) = I_0 \mu\tau \frac{V}{W^2} \left\{ 1 - \frac{\mu\tau V}{W^2} (1-a) \left(1 - e^{-\frac{W^2}{\mu\tau V}} \right) \right\}, \quad (1)$$

where a is the parameter that measures the ratio of ohmic to blocking behavior of the metal contacts, where $a = 0$ and $a = 1$ correspond to a complete blocking contact and an ohmic contact, respectively.⁴⁰ For the h-BN devices studied here, the values of a are about 0.1, implying the contacts are mostly blocking type.

The $\mu\tau$ product for the as-grown sample was determined to be $2.4 \times 10^{-5} \text{ cm}^2/\text{V}$, which is nearly an order of magnitude lower compared to our previously reported values for 100 μm thick h-BN wafers.^{24,35} The $\mu\tau$ product measurement results again suggest a degradation in the crystalline quality of h-BN with increasing h-BN thickness. The presence of defects and stacking faults tends to increase in thicker h-BN samples, where existing defects can propagate and introduce additional defects in subsequent layers, leading to a deterioration in the crystalline quality of the growth-front than underneath layers. This interpretation corroborates with the XRD results in Fig. 1, showing the inclusion of t-BN domains in as-grown 1 mm thick h-BN. So,

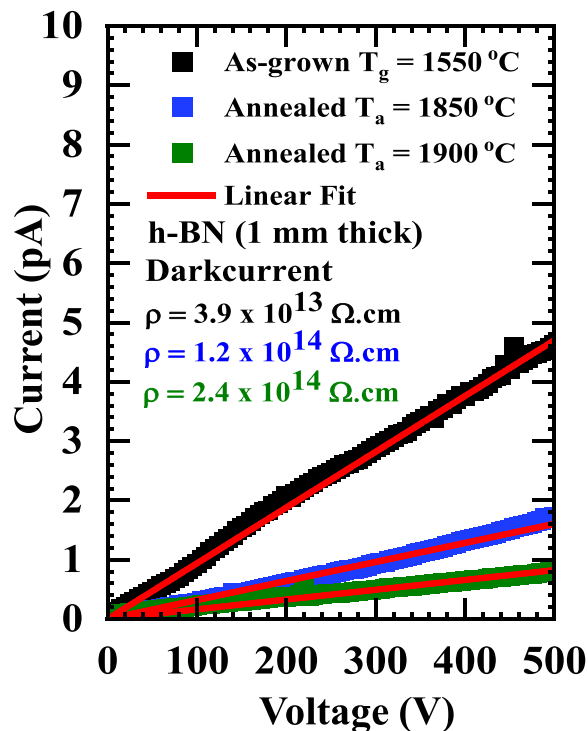


FIG. 2. Dark I–V characteristics of 1 mm thick h-BN wafers: as-grown, annealed at 1850 and 1900 °C.

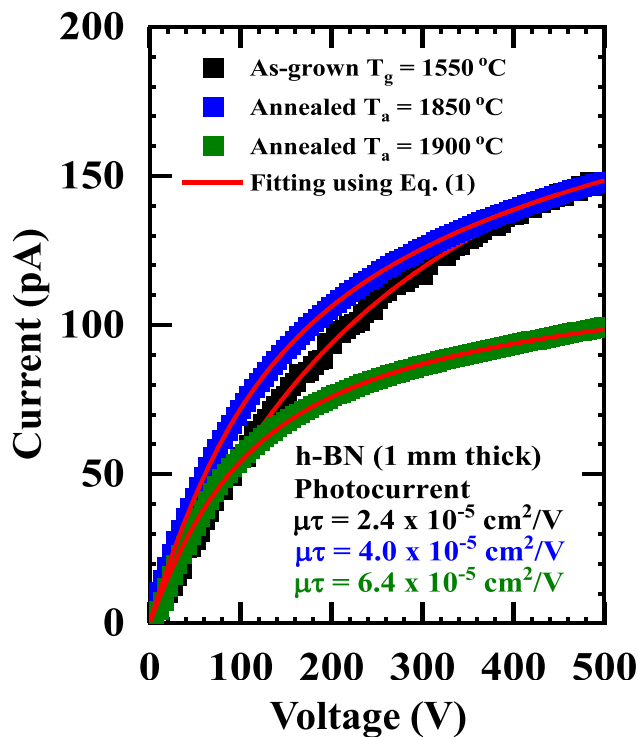


FIG. 3. I-V characteristics under photoexcitation for 1 mm thick h-BN lateral detectors fabricated using as-grown (black squares), annealed at 1850 °C (blue squares) and 1900 °C (green squares) samples.

presently, a trade-off between material quality and thickness must be considered when utilizing devices that incorporate thick h-BN wafers. Figure 3 (blue and green squares) show improvement of $\mu\tau$ products through annealing at high temperatures, with a $\mu\tau$ product reaching $6.4 \times 10^{-5} \text{ cm}^2/\text{V}$ for the h-BN sample annealed at 1900 °C. The annealing process contributes to an increase in the $\mu\tau$ value of h-BN by improving crystalline quality through the reduction of t-phase domains and native defects. This enhancement in material quality leads to a higher $\mu\tau$ value for h-BN, highlighting the significance of the annealing process in optimizing the performance of devices incorporating thick h-BN wafers.

Fast neutron detection performance for the fabricated devices was measured in response to fast neutrons emitted from an AmBe neutron source. The emission rate of the source at the time of measurement was 6.3×10^5 neutrons/s. The devices were put inside a metal box with the detection electronics. The detectors were placed 5 cm away from the neutron source. So, the neutron flux received at the detector surface was 2000 neutrons/cm²s. The detectors were operated in such a way as to perform particle counting and pulse height spectrum analysis, as we have done for h-BN thermal neutron detectors.^{20–26} The detection electronics include a charge-sensitive pre-amplifier, a current amplifier, and a multi-channel analyzer (MCA).^{20–26} Pulse height spectra were measured for the devices biased at a voltage of $V_B = 450$ V and are shown in Fig. 4.

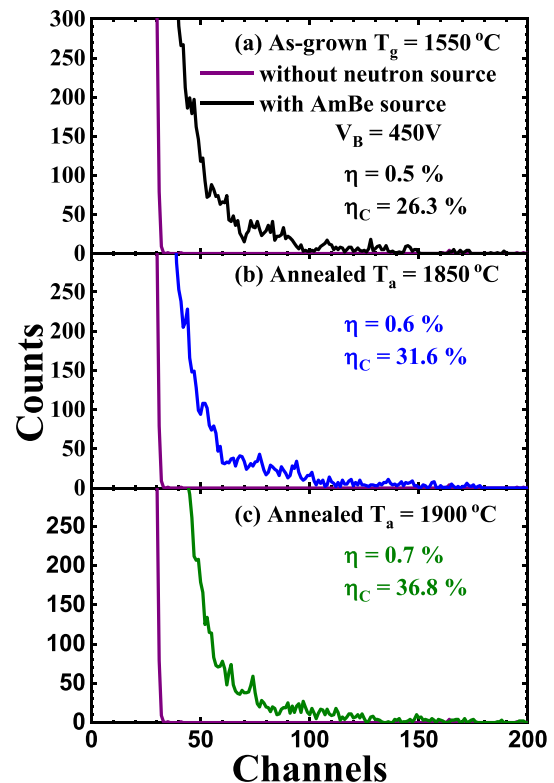


FIG. 4. Pulse height spectra measured at $V_B = 450$ V for 1 mm thick h-BN neutron detectors fabricated using (a) as-grown, annealed at (b) 1850 and (c) 1900 °C samples. The background signals (pulse height spectra in the absence of neutron source) are also plotted (purple curves).

The neutron detection efficiency (η) and charge collection efficiency (η_C) of the samples were then measured for each sample based on the pulse height spectra. Neutron detection efficiency (η) was determined by calculating the ratio of the count rate per unit area of the detector to the neutron flux at the detector position. The mean free path (λ) for neutrons emitted from the AmBe source in h-BN was measured to be 5.2 cm.²⁶ Utilizing this value, the intrinsic efficiency of a 1 mm thick h-BN neutron detector was calculated as $1 - \exp(-d/\lambda) = 1 - \exp(-0.1/5.2) = 1.9\%$. The charge collection efficiency (η_C) is derived from the ratio of the measured neutron detection efficiency to the intrinsic efficiency of a device with a specific thickness. Therefore, η_C for a neutron detector serves as an indicator of the overall quality of the material used in the devices. The device constructed using the as-grown h-BN exhibited a charge collection efficiency (η_C) value of 26.3%, as depicted in Fig. 4(a). Figures 4(b) and 4(c) demonstrate notable enhancements in the charge collection efficiencies for devices fabricated from annealed h-BN compared to the as-grown sample, with further improvement observed with increasing annealing temperatures. Specifically, the measured η and η_C values were, respectively, 0.6% and 31.6% for the detector fabricated using the 1850 °C annealed sample, and 0.7% and 36.8% for the detector fabricated using the 1900 °C annealed sample. The neutron detection performance of h-BN detectors is significantly improved through thermal annealing, as the annealed samples exhibit

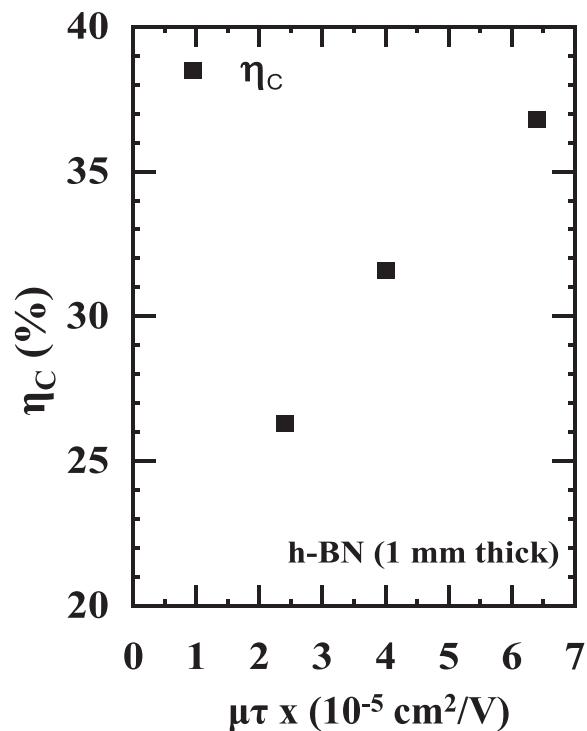


FIG. 5. Plot of the charge collection efficiency (η_c) of h-BN fast neutron detectors vs the $\mu\tau$ product.

improved crystalline quality and electronic transport properties, as evidenced by XRD, I-V characteristics in the dark and under photoexcitation, and the $\mu\tau$ products characterization results.

The $\mu\tau$ product, which encompasses information about carrier mobility and defect density, is a key parameter for determining the charge collection efficiency. From the measured η_c and $\mu\tau$ product values, Fig. 5 plots the correlation between η_c and $\mu\tau$, which clearly indicates that the $\mu\tau$ product is a significant figure of merit (FOM) for h-BN detectors. In addition to the $\mu\tau$ product, the detector thickness is the most important parameter for accommodating the large neutron mean free path in h-BN. This parallels the situation in solar cells, where the absorption coefficient and $\mu\tau$ product are key FOMs that influence solar cell performance.^{41,42}

In summary, 1 mm thick h-BN wafers were grown using HVPE and subsequently thermally annealed in N_2 gas at temperatures surpassing the growth temperature. XRD analysis revealed an enhancement in crystalline quality following high-temperature thermal annealing. Neutron detectors were then produced from both the 1 mm thick as-grown and annealed h-BN samples.

I-V characteristic measurements conducted in the dark conditions and under photoexcitation on devices constructed with annealed h-BN exhibited enhanced electrical resistivity and transport properties. Fast neutron detection efficiency measurements using an AmBe source demonstrated enhanced charge collection efficiencies and overall detection efficiencies for the annealed samples. While post-growth annealing is a simpler process compared to optimizing HVPE growth, our findings suggest its significant role in achieving improved material

quality and enhanced performance in electronic devices and neutron detectors fabricated from HVPE-grown quasi-bulk h-BN.

The information, data, or work presented herein was funded in part by the Advanced Research Projects Agency-Energy (ARPA-E), U.S. Department of Energy, under Award No. DE-AR0001552, monitored by Dr. Olga Spahn and Dr. Eric Carlson. The views and opinions of authors expressed herein do not necessarily state or reflect those of the United States Government or any agency thereof. Jiang and Lin are grateful to the AT&T Foundation for the support of Ed Whitacre and Linda Whitacre endowed chairs.

AUTHOR DECLARATIONS

Conflict of Interest

The authors have no conflicts to disclose.

Author Contributions

N. K. Hossain: Data curation (equal); Formal analysis (equal); Investigation (equal); Methodology (equal); Software (equal); Validation (equal); Visualization (equal); Writing – original draft (equal). **G. Somasundaram:** Data curation (equal); Formal analysis (equal); Investigation (equal); Methodology (equal); Software (equal); Validation (equal); Visualization (equal). **Z. Alemoush:** Data curation (equal); Formal analysis (equal); Investigation (equal); Methodology (equal); Software (equal); Validation (equal); Visualization (equal). **J. Li:** Data curation (equal); Formal analysis (equal); Investigation (equal); Methodology (equal); Project administration (equal); Resources (equal); Software (equal); Supervision (equal); Validation (equal); Visualization (equal). **J. Y. Lin:** Conceptualization (equal); Data curation (equal); Formal analysis (equal); Funding acquisition (equal); Investigation (equal); Methodology (equal); Project administration (equal); Resources (equal); Supervision (equal); Validation (equal); Visualization (equal); Writing – original draft (equal); Writing – review & editing (equal). **H. X. Jiang:** Conceptualization (equal); Data curation (equal); Formal analysis (equal); Funding acquisition (equal); Investigation (equal); Methodology (equal); Project administration (equal); Resources (equal); Supervision (equal); Validation (equal); Visualization (equal); Writing – original draft (equal); Writing – review & editing (equal).

DATA AVAILABILITY

The data that support the findings of this study are available within the article.

REFERENCES

- ¹S. Nakamura, T. Mukai, and M. Senoh, *Appl. Phys. Lett.* **64**, 1687 (1994).
- ²H. Amano, N. Sawaki, I. Akasaki, and Y. Toyoda, *Appl. Phys. Lett.* **48**, 353 (1986).
- ³H. X. Jiang and J. Y. Lin, *Nat. Electron.* **6**, 257 (2023).
- ⁴H. Amano, Y. Baines, E. Beam, M. Borga, T. Bouchet, P. R. Chalker, M. Charles, K. J. Chen, N. Chowdhury, R. Chu, and C. De Santi, *J. Phys. D* **51**, 163001 (2018).
- ⁵T. Sugino, K. Tanioka, S. K. S. Kawasaki, and J. S. J. Shirafuji, *J. Appl. Phys.* **36**, L463 (1997).
- ⁶K. Watanabe, T. Taniguchi, and H. Kanda, *Nat. Mater.* **3**, 404 (2004).
- ⁷Y. Hattori, T. Taniguchi, K. Watanabe, and K. Nagashio, *Appl. Phys. Lett.* **109**, 253111 (2016).

- ⁸N. Alem, R. Erni, C. Kisielowski, M. D. Rossell, W. Gannett, and A. Zettl, *Phys. Rev. B* **80**, 155425 (2009).
- ⁹L. Song, L. Ci, H. Lu, P. B. Sorokin, C. Jin, J. Ni, A. G. Kvashnin, D. G. Kvashnin, J. Lou, B. I. Yakobson, and P. M. Ajayan, *Nano Lett.* **10**, 3209 (2010).
- ¹⁰L. Britnell, R. V. Gorbachev, R. Jalil, B. D. Belle, F. Schedin, A. Mishchenko, T. Georgiou, M. I. Katsnelson, L. Eaves, S. V. Morozov, and N. M. R. Peres, *Science* **335**, 947 (2012).
- ¹¹R. Bourrellier, S. Meuret, A. Tararan, O. Stéphan, M. Kociak, L. H. Tizei, and A. Zobelli, *Nano Lett.* **16**, 4317 (2016).
- ¹²T. Ishii and T. Sato, *J. Cryst. Growth* **61**, 689 (1983).
- ¹³K. Watanabe, T. Taniguchi, T. Niyama, K. Miya, and M. Taniguchi, *Nat. Photonics* **3**, 591 (2009).
- ¹⁴T. Taniguchi and K. Watanabe, *J. Cryst. Growth* **303**, 525 (2007).
- ¹⁵N. D. Zhigadlo, *J. Cryst. Growth* **402**, 308 (2014).
- ¹⁶S. Liu, R. He, Z. Ye, X. Z. Du, J. Y. Lin, H. X. Jiang, B. Liu, and J. H. Edgar, *Cryst. Growth Des.* **17**, 4932 (2017).
- ¹⁷T. B. Hoffman, B. Clubine, Y. Zhang, K. Snow, and J. H. Edgar, *J. Cryst. Growth* **393**, 114 (2014).
- ¹⁸J. Li, X. K. Cao, T. B. Hoffman, J. H. Edgar, J. Y. Lin, and H. X. Jiang, *Appl. Phys. Lett.* **108**, 122101 (2016).
- ¹⁹G. F. Knoll, *Radiation Detection and Measurement*, 4th ed. (John Wiley & Sons, Hoboken, NJ, 2010).
- ²⁰A. Maity, S. J. Grenadier, J. Li, J. Y. Lin, and H. X. Jiang, *Appl. Phys. Lett.* **114**, 222102 (2019).
- ²¹A. Maity, T. C. Doan, J. Li, J. Y. Lin, and H. X. Jiang, *Appl. Phys. Lett.* **109**, 072101 (2016).
- ²²S. J. Grenadier, A. Maity, J. Li, J. Y. Lin, and H. X. Jiang, *Semiconductors and Semimetals* (Elsevier, 2021), Vol. 107, Chap. 12, p. 393.
- ²³A. Maity, S. J. Grenadier, J. Li, J. Y. Lin, and H. X. Jiang, *Appl. Phys. Lett.* **116**, 142102 (2020).
- ²⁴Z. Alemoush, A. Tingsuwatit, A. Maity, J. Li, J. Y. Lin, and H. X. Jiang, *J. Appl. Phys.* **135**, 175704 (2024).
- ²⁵N. K. Hossain, A. Tingsuwatit, Z. Alemoush, M. Almohammad, J. Li, J. Y. Lin, and H. X. Jiang, *Appl. Phys. Express* **17**, 091001 (2024).
- ²⁶J. Li, A. Tingsuwatit, Z. Alemoush, J. Y. Lin, and H. X. Jiang, *APL Mater.* **13**, 011101 (2025).
- ²⁷Y. Kumagai, T. Yamane, and A. Koukitu, *J. Cryst. Growth* **281**, 62 (2005).
- ²⁸Y. Kumagai, K. Goto, T. Nagashima, R. Yamamoto, M. Bockowski, and J. Kotani, *Appl. Phys. Express* **15**, 115501 (2022).
- ²⁹S. H. Lee, H. Jeong, O. F. N. Okello, S. Xiao, S. Moon, D. Y. Kim, G. Y. Kim, J. I. Lo, Y. C. Peng, B. M. Cheng, and H. Miyake, *Sci. Rep.* **9**, 10590 (2019).
- ³⁰F. Liu, X. Rong, Y. Yu, T. Wang, B. W. Sheng, J. Q. Wei, S. F. Liu, J. J. Yang, F. Bertram, F. J. Xu, X. L. Yang, Z. H. Zhang, Z. X. Qin, Y. T. Zhang, B. Shen, and X. Q. Wang, *Appl. Phys. Lett.* **116**, 142104 (2020).
- ³¹X. Z. Du, J. Li, J. Y. Lin, and H. X. Jiang, *Appl. Phys. Lett.* **111**, 132106 (2017).
- ³²K. Nakamura, *J. Electrochem. Soc.* **133**, 1120 (1986).
- ³³M. Chubarov, H. Pedersen, H. Högberg, J. Jensen, and A. Henry, *Cryst. Growth Des.* **12**, 3215 (2012).
- ³⁴A. Rice, A. Allerman, M. Crawford, T. Beechem, T. Ohta, C. Spataru, J. Figiel, and M. Smith, *J. Cryst. Growth* **485**, 90 (2018).
- ³⁵Z. Alemoush, N. K. Hossain, A. Tingsuwatit, M. Almohammad, J. Li, J. Y. Lin, and H. X. Jiang, *Appl. Phys. Lett.* **122**, 012105 (2023).
- ³⁶M. A. McKay, J. Li, J. Y. Lin, and H. X. Jiang, *J. Appl. Phys.* **127**, 053103 (2020).
- ³⁷A. Tingsuwatit, J. Li, J. Y. Lin, and H. X. Jiang, *Appl. Phys. Express* **15**, 101003 (2022).
- ³⁸Y. Kobayashi and T. Akasaka, *J. Cryst. Growth* **310**, 5044 (2008).
- ³⁹Z. Alemoush, A. Tingsuwatit, J. Li, J. Y. Lin, and H. X. Jiang, *Crystals* **13**, 1319 (2023).
- ⁴⁰A. Tingsuwatit, N. K. Hossain, Z. Alemoush, M. Almohammad, J. Li, J. Y. Lin, and H. X. Jiang, *Appl. Phys. Lett.* **124**, 162105 (2024).
- ⁴¹N. Beck, N. Wyrsh, C. Hof, and A. Shah, *J. Appl. Phys.* **79**, 9361 (1996).
- ⁴²P. Kaienburg, L. Krückemeier, D. Lübke, J. Nelson, U. Rau, and T. Kirchartz, *Phys. Rev. Res.* **2**, 023109 (2020).